Supplementary Materials: Flux-Activated Resonant Control of a Bosonic Quantum Memory

Fernando Valadares,[1,*] Aleksandr Dorogov,[1,*] Tanjung Krisnanda,[1] May Chee Loke,[1] Ni-Ni Huang,[1] Pengtao Song,[1,†] and Yvonne Y. Gao[1,2,‡]

[1] *Centre for Quantum Technologies, National University of Singapore, Singapore*
[2] *Department of Physics, National University of Singapore, Singapore*

(Dated: March 11, 2026)

I. DEVICE DESIGN

The standard bosonic cQED architecture consists of a high-Q bosonic mode hosted in a 3D superconducting cavity with convenient control and measurement tools provided by an on-chip ancillary transmon and a planar low-Q readout resonator. Our device extends this design by integrating fast-flux tunability without compromising long cavity lifetimes.

These flux control features are achieved by combining coplanar waveguide (CPW) and microstrip line architectures. We show the details of the circuit in Fig. S1. The tunable transmon is designed in a microstrip geometry, allowing it to have a large dipole moment that couples strongly to the cavity. The SQUID loop of the transmon is inductively coupled to an on-chip coil biased by a CPW flux line. The flux line is designed with an integrated microwave low-pass filter that mitigates cavity and transmon photon loss.

In this section, we explain the technical specifications and design considerations of the tunable transmon and the flux line control.

A. Tunable transmon with asymmetric SQUID

Standard transmon [1] qubits feature nonlinear inductance implemented as a Josephson junction, leading to anharmonic oscillator spectrum where one can isolate two-dimensional computational subspace with the transition frequency ω_{T} given by

$$\hbar\omega_{\mathrm{T}} = \sqrt{8E_C E_J} - E_C, \tag{1}$$

where E_J and E_C stand for Josephson and capacitive energies, respectively.

In order to make such a qubit tunable, single Josephson junction should be replaced by a loop with two junctions in parallel, forming a DC-SQUID. Magnetic flux Φ_e threaded through the SQUID loop effectively changes the value of the inductance and, therefore, the qubit frequency, according to

$$\hbar\omega_{\mathrm{T}} = \sqrt{8E_C \cdot 2E_J|\cos\varphi_e|} - E_C, \tag{2}$$

where E_J is the Josephson energy of a single junction, $\varphi_e = \pi\frac{\Phi_e}{\Phi_0}$ the normalised flux , and Φ_0 the magnetic flux quantum. Typical spectrum of ω_{T} as a function of the applied magnetic flux is shown in Fig. S2(a).

In such tunable devices, noise in the DC bias or in the magnetic environment leads to the fluctuations of the magnetic flux. This, in turn, varies the transmon frequency and leads to significant limitations on the T_2 lifetime. Thus, it is beneficial to operate at the sweetspots, where the qubit is first-order insensitive to the flux noise. At other bias points, the qubit suffers rapidly increasing dephasing.

This sensitivity to the flux noise can be quantified as $\frac{\partial\omega_{\mathrm{T}}}{\partial\Phi_e}$, i.e. how much the qubit frequency reacts to the fluctuations of the magnetic flux due to the noise. From Eq. (2),

$$\frac{\partial\omega_{\mathrm{T}}}{\partial\Phi_e} = -\frac{\pi^2}{\Phi_0}\sqrt{2\frac{E_C\cdot 2E_J}{h^2}}\frac{\sin 2\varphi_e}{\cos^{\frac{3}{2}}\varphi_e}. \tag{3}$$

The sensitivity to the flux noise grows rapidly outside of the sweetspots due to the strong dependence of frequency on the applied flux bias. Here, we intentionally suppress this dependency by making the two junctions asymmetric, i.e. having different Josephson energies [2]. The extent of asymmetry is expressed as

$$\gamma = \frac{E_{J2}}{E_{J1}}, \tag{4}$$

where E_{J1} and E_{J2} are Josephson energies of the junctions and $\gamma > 1$ without loss of generality.

Naturally, the spectrum of the asymmetric transmon will also depend on the parameter γ:

$$\hbar\omega_{\mathrm{T}} = \sqrt{8E_C\cdot E_{J1}\sqrt{\gamma^2+2\gamma\cos 2\varphi_e+1}} - E_C. \tag{5}$$

We calculate the flux noise sensitivity analogously to Eq. (3) using Eq. (5) and obtain

$$\frac{\partial\omega_{\mathrm{T}}}{\partial\Phi_e} = -\frac{\pi^2}{\Phi_0}\sqrt{\frac{2E_C E_{J1}}{h^2}}\frac{4\gamma\sin 2\varphi_e}{\left(\gamma^2+2\gamma\cos 2\varphi_e+1\right)^{\frac{3}{4}}}. \tag{6}$$

* Contributed equally to this work
† Current address: School of Automation Science and Engineering, Xi'an Jiaotong University, Xi'an 710049, China
‡ Corresponding author: yvonne.gao@nus.edu.sg

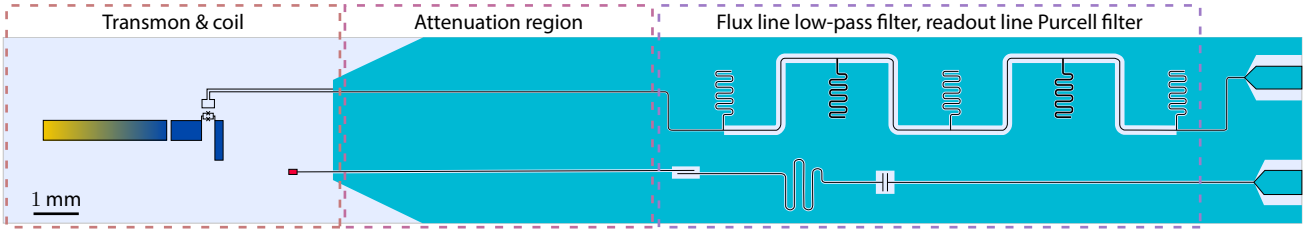

FIG. S1. **Chip schematic**. It features ancilla DC-SQUID transmon, low-Q readout resonator with Purcell filter, and on-chip flux line with microwave low-pass filter

.

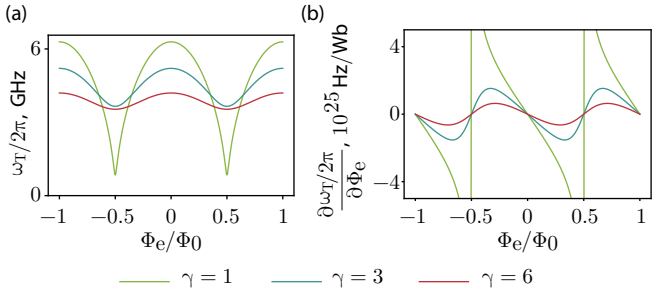

FIG. S2. **Reduced noise sensitivity of asymmetric SQUID transmons. (a)** Frequency response for variable junction asymmetry factors γ. **(b)** Calculated transmon frequency sensitivity to flux noise as a function of flux bias.

We present the simulated flux sensitivies obtained using Eq. (3) and Eq. (6) in Fig. S2(b). One can observe that more asymmetric transmons are less sensitive to the flux noise at the expense of a smaller frequency range. Therefore, for this particular device, we designed the SQUID to be asymmetric with a parameter $\gamma = 4.02$. The resulting frequency range is 5.894 - 7.634 GHz, as shown in Fig. S3(a).

It is worth mentioning that Eq. (2) and further analysis, strictly speaking, is only valid for the applied biasing DC current. In case of an AC flux drive, a more rigorous analysis [3, 4] must be applied to ensure an effective differential drive on the SQUID. The use of an asymmetric SQUID makes this optimisation more complicated. Although it is outside of the scope of this work, we are actively exploring alternative strategies that can balance the robustness to flux noise with the effective suppression of the common mode drive for future works that require clean AC modulation of the qubit frequency.

B. Flux line & on-chip microwave low-pass filter

The integration of on-demand adjustment of the transmon frequency without reducing the cavity coherence times had been an outstanding challenge for the bosonic cQED community. This feature is crucial as it enables powerful quantum information processing protocols [5, 6], as well as new opportunities for quantum simulation [7, 8] and quantum machine learning [9, 10]. However, initial attempts of the implementation of the broadband on-chip flux line encountered an issue of compromising cavity coherence [11]. In recent efforts, alternative ways of the flux delivery to the SQUID loop of the tunable ancilla have been explored [12–14]. However, these implementations tend to be difficult to manufacture reproducibly and offer limited bandwidth ($\sim$ 100 MHz).

In this work, we demonstrate the device that combines an on-chip flux line with both effective DC and AC flux delivery with a long-lived cavity. That is achieved by implementing heavy filtering of the flux line: we incorporate compact, third order Chebyshev low-pass filter [15] with cutoff frequency of 4 GHz on the same chip. To ensure effective filtering performance and protection of the cavity mode, we concatenate two such filters, with the stub Z_2 shared between the two, as depicted schematically in Fig. S1. We leverage the CPW architecture, which allows to reach necessary impedances in much more compact design compared to the microstrip analogue [16] and to fit both filtering stages on the 4.1 mm-wide chip. Moreover, our CPW architecture also suppresses cross-talk between the flux and readout modes hosted on the same chip.

The impedance values of the series inductances and stub capacitances used in our filter are listed in Tab. I, along with the corresponding CPW line dimensions.

Section	Impedance, Ω	Conductor width, μm	Gap width, μm
Z_0	50	11	5
Z_1	130	5	100
Z_2	81	5	13
Z_3	46	15	5

TABLE I. **Impedances of the 3-rd order Chebyshev low-pass filter**. Filter diagram is shown in Fig. 2 (a) of the main text.

The simulated response of the on-chip low-pass filter is shown in Fig. S3 (b). The attenuation at the cavity frequency (6.868 GHz) is 98 dB. For the entire transmon frequency band, the attenuation is at least 50 dB.

In this device, the SQUID area is 470 μm^2 (Fig. S4(a)), and the flux line coil loop is placed as close as 58 μm away from it to maximise the coupling (Fig. S4(b)). The mutual inductance of $L_{DC} = 0.387\,\Phi_0/\text{mA}$ is measured

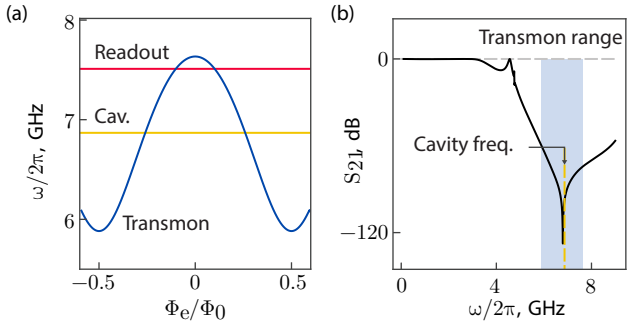

FIG. S3. **Filtering and spectrum**. **(a)** A spectrum of the transmon with asymmetric SQUID. Cavity and readout resonators frequency are shown. **(b)** S_{21} parameter of the cascaded low-pass 3-rd order Chebyshev filter.

from the transmon frequency perodicity with a DC bias. This allows us to reach full tunability (requires $\Phi_e = \frac{1}{2}\Phi_0$) with only 1.292 mA DC bias, which does not cause any measurable heating of the transmon.

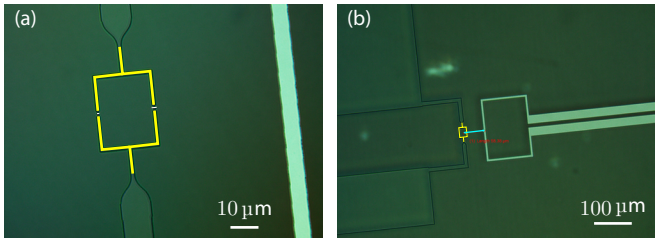

FIG. S4. **Optical images of the device after electron beam lithography**. **(a)** SQUID loop (yellow) with asymmetric junctions (white). **(b)** Flux line coil, biasing the transmon.

Furthermore, we incorporate a long constriction in the volume where the chip is housed, which we dub the "attenuation region". It considerably increases the cutoff frequency of the waveguide structure, enhancing the suppression of the cavity field traveling outside the ground plane. Hence, the cavity field can only propagate to the drive ports through the CPW mode, which is heavily filtered.

C. Readout and Purcell filter

Another advantage of the compactness of the CPW architecture, realised with the hybrid chip design, is its simplicity in integration of the readout resonator and the associated bandpass Purcell filter on the same chip. Our Purcell filter, which is shown in Fig. S1, is strongly coupled capacitively to both the readout resonator and the feed line. With this design, our readout resonator, which we place at 7.51 GHz, has coupling quality factor of $Q \approx 700$ without introducing any notable limitations on the transmon Q factor.

II. DEVICE FABRICATION

The device used in this study has considerably larger footprint compared to typical transmon chips used in bosonic cQED devices due to the ground plane and the flux line with low-pass microwave filter. For practical purposes, we only use EBL for patterning the transmon, while photolithography was used for all the other parts of the chip, as summarised in the Tab. II.

An optical microscope image of the SQUID right after EBL exposure is shown in Fig. S4(a).

Step 1: alignment markers

The fabrication of the device begins with the cleaning of a 2-inch C-plane sapphire wafer by sonicating in N-Methyl-2-pyrrolidone (NMP) and methanol for 4 minutes each, followed by baking at 200°C for 5 minutes to remove any residual chemicals molecules. Following this, the wafer is cooled down on a heat sink for 5 minutes. After that we spincoat two layers of the EBL resists: 550 nm of MMA (8.5) MAA EL13 and 250 nm of 950k PMMA A4. Each of the spincoating rounds is followed by baking for 5 minutes at 200°C. Next, we sputter an anti-charging gold layer of ∼10 nm thickness. We then expose the alignment markers using Raith EBPG 5200+ EBL system with the dose 750 μC/cm^2. Subsequently, we etch gold using KI gold etchant and develop the exposed pattern with 3:1 IPA:H2O at 6°C for 2 minutes.

To clean leftover resist before the metal deposition, we apply etching for 60 seconds in Ar (85 %) – O_2 (15 %) environment and evaporate 115 nm of Nb using Angstrom Engineering double-angle evaporation system. We perform lift-off via soaking the wafer in NMP at 90°C for 3 hours and then sonicating in NMP, acetone and methanol for 3 minutes each.

Step 2: readout line, flux line, ground plane

We start by spincoating ∼ 1 μm of AZ1512 photoresist and baking for 1 minute at 100°C. Once this is completed, we expose the large features with 405 nm laser in Durham Magneto Optics MicroWriter ML3 Pro. Following this, we develop the exposed resist with MF-319 developer for 40 seconds and evaporate 100 nm of Al. Etching for 30 seconds and the evaporation itself are followed by capping in a 20 mbar O_2 environment for 20 minutes. To lift-off, we soak the wafer in NMP at 80°C for 4 hours and sonicate in NMP, acetone and methanol 3 minutes each.

Step 3: transmon with SQUID

Finally, we perform standard electron beam lithography to make the trasmon qubit. The junctions are fabricated using the bridge-free technique, presented in [17].

# of lithography step	Exposure method	Material	Written feature
1	EBL	Nb	Alignment markers
2	Photolithography	Al	Readout line, flux line, ground plane
3	EBL	Al	Transmon with the SQUID loop

TABLE II. **Summary of the main fabrication steps**. A breakdown of the processes used in fabricating respective on-chip features.

We then perform double-angle evaporation by first etching the resist at ±20° angles for 15 seconds each. Subsequently, we deposit two layers of Al with thicknesses of 20 nm and 40 nm, separated by oxidation for 20 minutes in 20 mbar O_2 environment. We finish the evaporation by capping in 20 mbar O_2 environment for 20 minutes.

III. DEVICE ASSEMBLY AND WIREBONDING

A. Package

Conventional bosonic cQED architecture usually uses a monolith package, made of high-purity aluminium, to minimise seam loss [18, 19]. The chip hosting the ancillary elements is inserted into a waveguide to couple capacitively to the cavity mode and the other end of the chip is held by a clamp, which is, in turn, attached to the main package. However, this approach is not suitable for the device we use here. The on-chip ground plane and requirement for wirebonding necessitate a seam placed near the cavity wall.

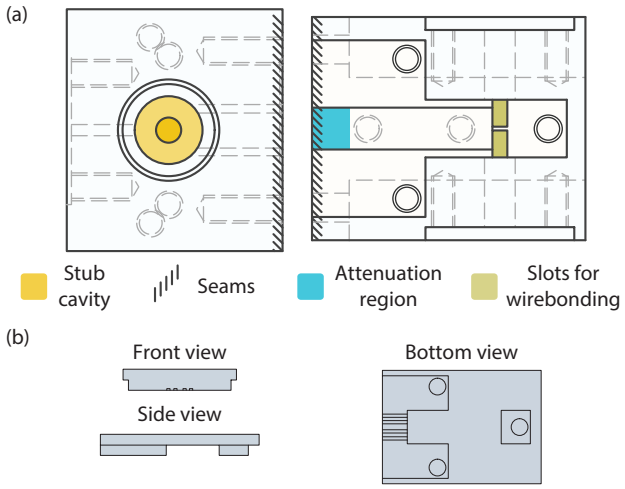

FIG. S5. **Design of the superconducting package**. **(a)** Top view of the main body and the bottom clamp. **(b)** Design of the top clamp with engineered constrictions.

Hence, our superconducting package was carefully redesigned to accommodate these requirements. Unlike conventional architecture, our package consists of three separate parts. The main body contains the cavity and the circular waveguide, where the transmon is inserted (Fig. S5(a)). This part is made of 4N6 aluminium to ensure the long lifetime of the coaxial $\lambda/4$-cavity.

The clamping structure consists of two pieces, the bottom and top clamps. As we expect the high-Q cavity mode field to be weak in the clamps volume, these parts are made of 6061 aluminium alloy to allow more precise machining and mechanical robustness.

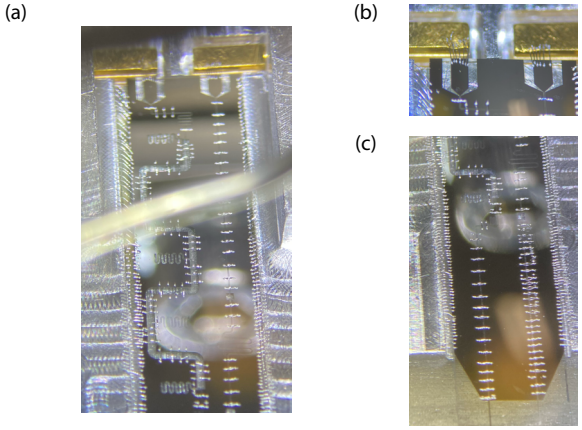

FIG. S6. **Wirebonding**. **(a)** Image of the chip on the bottom clamp after wirebonding. **(b)** Connection of the on-chip lines to th SMA ports. **(c)** Bond wires and galvanic connection between the on-chip ground plane and the aluminium bottom clamp are also realised with wirebonding.

The top clamp functions as a lid that covers the chip and shields it from the environment. Importantly, it features a 4mm-long extrusion (Fig. S5(b)), which blocks the cavity field from propagating towards SMA ports outside the heavily filtered CPW line.

The bottom clamp features a 0.5 mm-deep pocket, where the chip is located (Fig. 2(a), main text). We use wirebonding to connect the on-chip ground to the surface of the clamp surrounding it (Fig. S6(a),(c)). The package is then mounted on the MXC flange of the dilution refrigerator, effectively connecting on-chip ground plane to the common fridge ground. Similarly, we use wirebonding to galvanically connect the flux and readout line terminals to flat beryllium-copper pins, that are connected to SMA ports (Fig. S6(b)). The drive signals are supplied to the SMA ports through the coaxial lines of the dilution refrigerator.

Seam losses estimation

To avoid deterioration of the cavity lifetime, our design places the seam as far as possible from the cavity. In order to estimate cavity Q-factor due to the seam loss, we integrated the cavity field over a 0.4 mm-wide ribbon along the seam. Even though we don't have exact data on the loss tangent of the seam, we could use that method to optimise the design based on the relative changes of the cavity Q.

Distancing the seam comes at the cost of increasing the separation between the cavity and the transmon, which could lead to decreasing their coupling strength g. In order to mitigate this effect, we implemented a microstrip structure to extend the transmon field and recover some of the capacitive coupling, similar to the design used in Ref. [13].

B. Assembly

We begin the assembly by putting a small amount of the Apiezon N cryogenic vacuum grease on the surface of the bottom clamp. We then place the chip on top and press slightly with a wooden part of the cotton swab. The grease is only present at the back part of the chip, far from the cavity.

Next, the top clamp is placed on top of the chip and fastened with 3 screws. At this point, the chip is extruding out of the clamp slightly. Finally, the cavity body and the clamping pieces are attached together with the two screws located at the bottom of the clamp.

To improve the contact at the seam in our package, we put indium wire in between the cavity and the clamping parts. The quality of this joint can be further improved with welding [20] or more advanced surface treatment [21].

Before mounting the device on the MXC flange of the dilution refrigerator, we cover all the seams between the parts with aluminium tape to ensure that the package is light-tight.

IV. CALIBRATION OF TRANSITIONS

The Jaynes-Cummings ladder has a rich spectrum of transitions. We calibrate the frequency and amplitude of each transition by preparing the system in one of the adjacent states and then performing spectroscopy and Rabi oscillation experiments.

For example, to calibrate the $|3-\rangle \leftrightarrow |4+\rangle$ transition the system is initialised in $|3-\rangle$ with the cavity and transmon on resonance. The transmon is then driven by a pulse with variable frequency and subsequently adiabatically detuned from the cavity. Finally, the transmon, now dispersively coupled to the cavity, is used to measure the parity using a standard Ramsey sequence. A change in parity indicates that drive has excited one of the four allowed transitions to states $|2\pm\rangle$ or $|4\pm\rangle$, which appear as four well-resolved features in the spectroscopy diagram. The desired $|3-\rangle \leftrightarrow |4+\rangle$ transition is identified as the one with highest frequency, in accordance with the theory.

After the transition frequency is identified, the amplitudes of excitation pulses are calibrated with power Rabi experiments. A gaussian pulse with standard deviation σ and a total duration of 4σ is applied to the transmon line with variable amplitude. The amplitude corresponding to a π pulse is the point in which the parity of the system is changed from odd to even. This experiment allows us to calculate the Rabi frequency Ω_s of the effective drive $\frac{\Omega_s}{2}|4+\rangle\langle 3-|$. The corresponding frequencies and amplitudes of each JC transition are calibrated using this method and summarised in Tab. III.

Transition	$\omega_s/2\pi$ (GHz)	$\Omega_s/2\pi$ (MHz)	σ (ns)
$\|0\rangle \leftrightarrow \|1+\rangle$	6.8809	29.0	68
$\|0\rangle \leftrightarrow \|1-\rangle$	6.8566	25.5	52
$\|1-\rangle \leftrightarrow \|2+\rangle$	6.8987	22.3	44
$\|1+\rangle \leftrightarrow \|2-\rangle$	6.8402	18.9	48
$\|2-\rangle \leftrightarrow \|3+\rangle$	6.9074	24.1	44
$\|2+\rangle \leftrightarrow \|3-\rangle$	6.8315	19.4	32
$\|3-\rangle \leftrightarrow \|4+\rangle$	6.9142	25.9	44
$\|3+\rangle \leftrightarrow \|4-\rangle$	6.8246	22.0	24
$\|4-\rangle \leftrightarrow \|5+\rangle$	6.9201	25.5	32
$\|5+\rangle \leftrightarrow \|6-\rangle$	6.8143	22.7	—
$\|6-\rangle \leftrightarrow \|7+\rangle$	6.9291	24.5	—

TABLE III. **Calibration of the parameters of the transitions drives.** The table shows the frequency of each relevant transition and its respective maximum Rabi frequency Ω_s. Ω_s is defined as the coefficient of the $\frac{\Omega_s}{2}|(N+1)\mp\rangle\langle N\pm|$ matrix element when activated through the transmon drive. The parameter σ is the standard deviation of the Gaussian π pulse calibrated for each transition, with total duration of 4σ. The length of the $|5+\rangle \leftrightarrow |6-\rangle$ and $|6-\rangle \leftrightarrow |7+\rangle$ transitions were not optimised.

We use this method to calibrate the gaussian excitation pulses used for cavity state preparation in the main text. The σ of each pulse was swept while tracking the parity of the state after a 2π rotation. The ideal σ is such that the parity of the final state is as close as possible to the parity of the initial state. This corresponds to a compromise between the leakage and decoherence errors that affect short and long pulses, respectively.

V. GATE TIME AND LIFETIME COMPARISON

Here, we compare the resonant JC regime that we implemented to the well-known universal control techniques such as selective number-dependent arbitrary phase (SNAP) gate [22, 23], gradient ascent pulse engineering (GRAPE) [24], and echoed conditional displacement (ECD) [25] in the dispersive regime. We will make the comparison in two folds: in terms of the gate dura-

tion for generating arbitrary states on the cavity state up to Fock state $|n\rangle$ and in terms of effective lifetime of the system.

First, let us note that the dispersive regime is a special case of the JC regime where the detuning is much larger than the coupling g ($\Delta = \omega_q - \omega_c \gg g$). In this regime, the main coupling term reads $\hat{H}_{\rm int} = -\chi \hat{a}^\dagger \hat{a} |e\rangle\langle e|$, where $\chi \approx g^2/\Delta$. Notably, the dispersive regime can be further subdivided into two classes based on the ratio between χ and the fastest decoherence rate in the system, $\max(\Gamma_\phi, \Gamma_1, \kappa)$, characterising ancilla dephasing $T_\phi = 1/\Gamma_\phi$ and relaxation $T_1 = 1/\Gamma_1$, as well as cavity lifetime $T_{1,\rm cav} = 1/\kappa$. In the strong dispersive regime, the bare nonlinearity χ is considerably larger than $\max(\Gamma_\phi, \Gamma_1, \kappa)$, whereas in the weak dispersive regime $\chi \lesssim \max(\Gamma_\phi, \Gamma_1, \kappa)$. SNAP and GRAPE operate in the strong dispersive regime, where typically $\chi \sim 1\,\text{MHz}$. For SNAP, by driving the qubit at a certain frequency, an arbitrary phase can be imparted on the cavity Fock state $|n\rangle$ selectively, which essentially sets the gate time as $T \sim 1/\Omega$, where Ω is the strength of the qubit drive [22]. For generating an arbitrary state within Fock state $|n\rangle$, it would involve applying the SNAP gate n times, which gives $T \sim n/\Omega$ as the total gate time. However, with multi-tone qubit drives, the operation imparting arbitrary phases for all relevant Fock states can be applied simultaneously, making the gate time faster: $T_{\rm SNAP} \sim 1/\Omega$, which is independent of n. And it is important to point out that for SNAP, selectivity demands $\Omega \ll \chi$, and therefore $T_{\rm SNAP} \sim 1/\Omega \gg 1/\chi$. Another technique, GRAPE, does not require the strict selectivity of SNAP. Also, the qubit and cavity drives can be simultaneously applied while the qubit and cavity are dispersively coupled. This way, GRAPE is more general compared to SNAP, i.e., the solution space for GRAPE contains that of SNAP. This makes the gate time for GRAPE often faster than multi-tone SNAP, which is set by the dispersive coupling strength $T_{\rm GRAPE} \sim 1/\chi \approx \Delta/g^2$ [26].

The technique of ECD, operating in the weak dispersive regime, enhances the nonlinearity in situ via applying strong resonant microwave drive to displace the bosonic mode far from the origin in the phase space. In this displaced frame, the dispersive four-wave-mixing interaction is transformed into three-wave-mixing, resulting in the interaction term resembling the resonant JC Hamiltonian: $\hat{H}_{\rm int}^{\rm DF} = \chi(\alpha\hat{a}^\dagger + \alpha^*\hat{a})\sigma_z/2$, where α is the displacement of the cavity in the phase space. Comparing $\hat{H}_{\rm int}^{\rm DF}$ to the Eq. (1) of the main text, one can conclude that ECD leverages the effective interaction strength $g_{\rm eff} = \chi\alpha$. This bosonic enhancement by a factor of α, though powerful, is limited by the criticial cavity photon number [27], leading to the upper bound of the enhanced interaction of $g_{\rm eff}^{\rm max} = \sqrt{\chi E_C/6\hbar}$, where E_C is the capacitive energy of the transmon, approximately equal to the transmon anharmonicity. For the typical transmon designs, $E_C/2\pi\hbar$ is in the range of $200 - 300$ MHz in order to suppress the charge noise. In Ref. [25], where $\chi/2\pi = 33$ kHz and $E_C/2\pi\hbar = 193$ MHz, $g_{\rm eff}^{\rm max} \approx 1$ MHz, which sets the lower bound for the gate time of one ECD gate to be $t_{\rm ECD} \geq 1/g_{\rm eff}^{\rm max}$. Furthermore, universal control in this regime involves sequential applications of ECDs and qubit rotations, where the complexity of applying an arbitrary gate of dimension n scales with the number of applications n.

On the other hand, protocol for generating arbitrary superpositions of Fock states has also been realised utilizing sequential off- and on-resonant (JC regime) qubit-cavity regimes [28, 29]. Here, each JC ladder transition $|e, n-1\rangle \leftrightarrow |g, n\rangle$ has a Rabi rate $\Omega\sqrt{n}$, making each step $t_n \sim 1/(g\sqrt{n})$ long. For an operation involving n ladders, the total gate time is approximately $T_{\rm JCS} = \sum_n t_n \sim \sqrt{n}/g$. Importantly, this protocol was further improved by incorporating qubit drives with multi-tone frequencies, which drive all relevant transitions at the same time [30], ultimately resulting in $T_{\rm JC} = \max_n t_n \sim 1/g$. If we compare this to the dispersive regime (GRAPE), we have $T_{\rm JC} \sim (g/\Delta) \times T_{\rm GRAPE}$. Considering that $g/\Delta \approx 0.05 - 0.2$, the gate time utilizing JC regime is $5 - 20$ times faster.

For effective lifetime comparison, let us assume that the major contribution comes from qubit energy decay and dephasing, where the corresponding lifetimes are denoted as T_1 and T_ϕ, since the cavity lifetime is normally much longer. For SNAP, GRAPE, and ECD, the qubit is utilised differently during a particular protocol. However, the error probabilities due to the qubit can be approximated in the same way. In particular, the error probability related to qubit decay is roughly estimated to be $\epsilon_1 \sim p_e \times T/T_1$, where p_e is the average probability of the qubit being in the excited state (when the decay happens) during the protocol. This approximation also applies for dephasing $\epsilon_2 \sim 2\sqrt{p_e p_g} \times T/T_\phi$, which is affecting the qubit state in superposition, the maximum of which happens for equal superposition $p_g = p_e = 0.5$, leading to maximum error $\sim T/T_\phi$. Therefore, the total error goes as $\epsilon \sim T(p_e/T_1 + 2\sqrt{p_e p_g}/T_\phi)$. One can define an effective lifetime for the system $T_{\rm sys}$ in relation to the error and total gate time as $\epsilon \sim T/T_{\rm sys}$ such that $T_{\rm sys} \sim (p_e/T_1 + 2\sqrt{p_e p_g}/T_\phi)^{-1}$.

In the case of the JC regime, as written in the main text the effective decay lifetime of the coupled system is approximately twice that of the qubit $2T_1$, while the dephasing (depolarisation) is T_ϕ, as the JC eigenstates contain equal superposition of the qubit's ground and excited states. Consequently, this results in effective lifetime $T_{\rm sys} \sim (1/(2T_1) + 1/T_\phi)^{-1}$ for the system. A comparison for the lifetime is generally hard to make since it is protocol specific. However, one can see that for average qubit probability $p_e \sim 0.5$ in the dispersive regime, the system lifetime is equal to the JC regime.

An important point worth stressing is that we detune the qubit after the protocol such that the qubit is decoupled from the cavity, and therefore the cavity's lifetime is back to its original value. Even though the resonant control protocol introduces the small overhead due to the time required to adiabatically detune the system from

resonance, this overhead is constant (does not scale with the gate complexity) and reasonably short even on the timescale of the current system lifetimes (~ 200 ns).

The resonant scheme achieves fast gate time without compromising the lifetime of the system. Therefore, we argue that the JC protocol that we implement here offers the most favourable strategy for universal control of a bosonic mode.

Our method can be further improved by exploring the deep-strong (DS) and ultra-strong (US) coupling regimes of the JC Hamiltonian, providing access to significantly higher values of coupling strength g. However, the rotating wave approximation of the quantum Rabi model [31], used in current analysis (see Eq. (1) of the main text), will not be applicable anymore in those regimes. Therefore, new strategies are to be developed for universal control of JC Hamiltonian in DS and US regimes.

Other methods, such as tailored nonlinear Hamiltonians beyond JC dynamics, can also be explored. For instance, the cubic interactions [32] have been demonstrated on a low-Q oscillator by directly terminating the planar cavity with a nonlinear element. The strong nonlinearity inherent to such bosonic mode allows operations on the timescale of tens of nanoseconds. However, such an element is not an effective quantum memory, as the nonlinearity cannot be dynamically decoupled from the cavity, leading to always-on high decoherence rate. Furthermore, this scheme can only operate in the bounded area of the phase space ($|\alpha| < 1.5$), outside of which the control is undermined by the static Kerr nonlinearity. Therefore, at this stage such an approach still requires further investigation in order to be a general-purpose tool to achieve universal control of a bosonic mode.

VI. PREPARATION OF ARBITRARY BOSONIC STATES

We used the resonant control protocol to demonstrate the preparation of arbitrary states in the cavity with an analytical control sequence. The sequence consisted of activating the sidebands sequentially using variable-amplitude, Gaussian-shaped pulses with 4σ duration, with the parameters given in the Tab. III. This method allows for straightforward preparation of any Fock state and their superpositions in the cavity, as shown in Fig. S7.

Due to the lack of appropriate quantum amplifier at the specific moment of this experiment, we don't have single-shot readout of the transmon. Thus, the parity signal was calibrated by comparing it to a 1D Wigner measurement of cavity vacuum $|0\rangle$, which is independently measured beforehand. The Wigner plots closely resemble the target states in shape, though with a reduction in contrast. This indicates that the state preparation is mostly limited by the transmon decoherence.

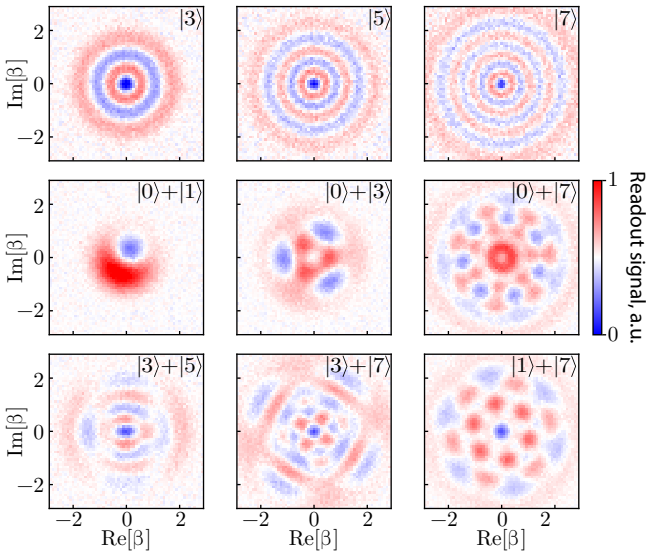

FIG. S7. **Qudit arbitrary state preparation.** Wigner plots showing diverse qudit states prepared by sequentially exciting sideband transitions in the Jaynes-Cummings ladder.

VII. ARBITRARY GATE ON LOGICAL STATES OF BINOMIAL ENCODING

As shown in Sec. VI, resonant control protocol enables arbitrary state preparation. Here, we show that an arbitrary gate on the logical states of binomial encoding of the lowest order [33] can be achieved within the framework of the resonant control protocol. This follows as Givens rotations can be utilized to realise $\hat{R}^{\mathrm{L}}_x(\theta)$, $\hat{R}^{\mathrm{L}}_y(\theta)$, and $\hat{R}^{\mathrm{L}}_z(\theta)$ on the subspace $\{|\downarrow\rangle^{\mathrm{L}} = |2\rangle, |\uparrow\rangle^{\mathrm{L}} = (|0\rangle + |4\rangle)/\sqrt{2}\}$. The rotations can be written explicitly in terms of Givens rotations as

$$\hat{R}^{\mathrm{L}}_x(\theta) = \hat{\mathcal{R}}_{0,2}(\zeta_1)\hat{\mathcal{R}}_{2,4}(\zeta_2)\hat{\mathcal{R}}_{0,2}(\zeta_1), \tag{7a}$$

$$\hat{R}^{\mathrm{L}}_y(\theta) = \hat{\mathcal{R}}^{-\pi/2}_{0,2}(\zeta_1)\hat{\mathcal{R}}^{\pi/2}_{2,4}(\zeta_2)\hat{\mathcal{R}}^{-\pi/2}_{0,2}(\zeta_1), \tag{7b}$$

$$\hat{R}^{\mathrm{L}}_z(\theta) = \hat{\mathcal{R}}_{0,4}(-2\theta), \tag{7c}$$

where the parameters $\zeta_1 = 2\arctan\left(\tan(\theta/4)/\sqrt{2}\right)$, $\zeta_2 = 4\arcsin\left(\sin(\theta/4)/\sqrt{2}\right)$, and the notation $\hat{\mathcal{R}}^{\gamma}_{n_A,n_B}(\alpha)$ means Givens rotation between the Fock states $|n_A\rangle$ and $|n_B\rangle$ by an angle α as described in the main text, where the pulse is phase-shifted by γ.

Thus, arbitrary control on the logical states of the binomial encoding is enabled via trivial combinations of the Givens rotations.

VIII. PARAMETRIC MODULATION

Although not required for the resonant control protocol, our device architecture is also capable of providing broadband parametric flux modulation of the SQUID.

We show this feature experimentally by using flux pumps to activate parametric resonances between the cavity and transmon with tunable strength. Sweeping the pump frequency ω_m around the transmon-cavity detuning of $\Delta \approx 85\,\mathrm{MHz}$ for a variable duration results in the continuous exchange of the transmon excitation with the cavity, as shown by the chevron pattern in Fig. S8(a). The resonant oscillations have a period of π/g_{eff}, where g_{eff} is the parametric coupling strength.

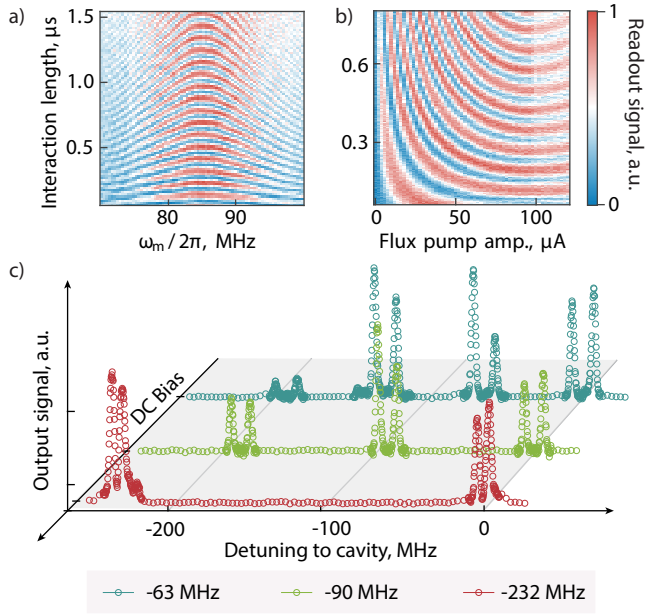

FIG. S8. **Protected flux-parametric modulation. (a)** Vacuum Rabi oscillations activated by a flux sideband. The transmon-cavity detuning is $\Delta = 85$ MHz. After being excited with a π pulse, a flux pump with $\omega_m/2\pi \approx \Delta$ creates a sideband that activates the photon exchange between transmon and cavity for a variable interaction time. **(b)** Resonant vacuum Rabi oscillations as a function of the flux pump amplitude. The speed of the Rabi oscillations can be continuously tuned in the $g_{\mathrm{eff}}/2\pi = 0 \div 6.57$ MHz range. **(c)** Transmon spectroscopy for the variable values of Δ under a flux pump $\varphi_e \propto \cos\left(2\pi\Delta t\right)$. The flux pump activates the parametric resonance between the transmon and the cavity, as seen from the frequency split that appears on every sideband due to the avoided crossing.

The parametric coupling strength g_{eff} can be tuned on demand by changing the flux pump amplitude. Fig. S8(b) shows that the resonant oscillations become faster with larger flux pump amplitude (expressed in units of current), corresponding to an increase in coupling strength. The pump amplitude I_p is estimated from the room-temperature input current after going through 26 dB attenuation and treating the flux line as a short. Fitting the oscillations to a cosine function for each pump amplitude indicates a variable $0 \leq g_{\mathrm{eff}} \leq 6.57\,\mathrm{MHz}$. However, increasing the pump amplitude beyond the maximum coupling point leads to lower g_{eff}. This is consistent with the expected analytical trend $g_{\mathrm{eff}} = g \times J_1(I_p/\nu)$, where g is the static coupling, J_1 is a Bessel function of the first kind and ν is proportionality factor [34].

The g_{eff} data extracted from Fig. S8(b) fits to the function $g_{\mathrm{eff}}/2\pi = 11.3\ \mathrm{MHz} \times J_1\left(I_p/53\,\mu\mathrm{A}\right)$, where I_p is in units of μA. The estimated coupling of $g = 11.3\,\mathrm{MHz}$ is close to the value of $12.2 \pm 0.1\,\mathrm{MHz}$ observed from the transmon-cavity avoided crossing. The factor ν can be calculated analytically using the formula

$$\nu = \left(\frac{2\pi}{\Phi_0}\frac{d\omega_T}{d\varphi_e}\frac{L}{\omega_m}\right)^{-1}, \tag{8}$$

where $\omega_T/2\pi = 6.783\,\mathrm{GHz}$ is the transmon parking frequency and L is the effective mutual inductance with the SQUID. From the fitting value of $\nu = 53\,\mu\mathrm{A}$ we can calculate $L = 0.211\,\Phi_0/\mathrm{mA}$, which is considerably lower than the DC bias mutual inductance of $L_{DC} = 0.387\,\Phi_0/\mathrm{mA}$. This lower tunability can be partially attributed to the flux pump not fully driving the differential mode of the SQUID loop [35]. In further device iterations, the mismatch can be mitigated by incorporating a common-mode rejection filter on the flux line [16].

We test strong parametric resonances with flux pumps at higher modulation frequency. This is shown with transmon spectroscopy experiments at different parking detunings $\Delta = 63$ to $232\,\mathrm{MHz}$ under a continuous flux pump with frequency $\omega_m = \Delta$. The pump creates flux sidebands at frequencies $\bar{\omega}_T + N\omega_m$, where the average transmon frequency $\bar{\omega}_T$ approximately coincides with the parking frequency ω_T for low pump amplitudes. In all spectroscopy plots (Fig. S8(c)), the rightmost feature corresponds to the $N = 1$ sideband, which coincides with the cavity frequency and presents a frequency split corresponding to their avoided crossing. The next feature to the left corresponds to the transmon average frequency ($N = 0$), and the lower $N = -1$ and $N = -2$ sidebands can be seen within range of the spectroscopy for some DC biases. All features display the same frequency splitting indicating the strong coupling of the $N = 1$ sideband to the cavity for pump frequencies as high as $232\,\mathrm{MHz}$.

IX. QUANTUM STATE RECONSTRUCTION

Here, we explain the procedure for reconstructing a quantum state, represented by its density matrix, with truncation dimension D, given the Wigner measurement data. An arbitrary D dimensional quantum state ρ is fully characterised by its $D^2 - 1$ independent real parameters, which we write in a vector form $\vec{Y}$. There are many choices for the parametrisation of ρ. We take the first $D - 1$ diagonal elements of ρ as well as the $D^2 - D$ real and imaginary off-diagonal (upper triangular) elements. This way, the vector $\vec{Y}$ consists of real elements, which fully characterise the density matrix ρ.

On the other hand, the Wigner measurement that we performed is expressed as $W(\alpha) = \mathrm{tr}(\hat{P}\hat{D}(\alpha)^\dagger\rho\hat{D}(\alpha))$ with $\hat{P} = e^{i\hat{a}^\dagger\hat{a}\pi}$ being the parity operator and grid-based

displacement points $\{\alpha\}$. Let us express all the Wigner data in a vector form $\vec{X}$. Consequently, the input state and Wigner data are related linearly, which can be written in a single matrix equation $\vec{X} = M\vec{Y} + \vec{V}$, where M and $\vec{V}$ denote a mapping matrix and a constant vector, which can easily be computed given the choice of displacements $\{\alpha\}$.

The state reconstruction is carried out in a few steps. First, we perform linear inversion (LI) to get the estimated state parameters $\vec{Y}_{\text{est}}$, given the Wigner measurement data $\vec{X}$: $\vec{Y}_{\text{est}} = M^{+}(\vec{X} - \vec{V})$, where $M^{+} = (M^{\dagger}M)^{-1}M^{\dagger}$ is the left Moore-Penrose pseudoinverse of the matrix M. Then, we construct the density matrix ρ_{LI} based on the estimated parameters. As errors are present in experiments, this density matrix might not be physical, i.e., it might contain negative eigenvalues. Thus, given ρ_{LI}, we employ Bayesian inference (details below) to obtain a posterior probability distribution that accurately represents experimental data. From this distribution, we can sample density matrices and compute the mean fidelity and its standard deviation.

A. Bayesian inference

A popular technique to obtain a physical density matrix from experimental data in the presence of noise is maximum likelihood (ML), which gives us the closest physical density matrix ρ_{ML} from the obtained density matrix ρ_{LI} via linear inversion [36]. However, it is statistically less accurate. For example, it often leads to ρ_{ML} having zero eigenvalues [37, 38]. This is an issue as zero eigenvalues are interpreted as zero probabilities if we were to measure in the corresponding basis, which is not a valid conclusion as we perform finite measurement repetitions.

To address this issue, we use Bayesian inference, which is a statistically more accurate approach. Through Bayes' rule, it gives us a posterior distribution, explicitly showing uncertainty, given the measured experimental data (ρ_{LI}). The posterior distribution allows us to sample any functions of ρ (including itself). For exact implementation of Bayesian inference, we follow an efficient protocol proposed in Ref. [39]. When implementing the protocol, we use the following parameters: $\alpha = 1$, which establishes a uniform prior as we do not assume initial preference for the density matrix; the variance of the pseudo-likelihood $\sigma = 1/N$ with $N = \# \cdot (D^2 - 1)$, where $\#$ is the number of experimental repetition; we also generate 2^{10} Markov Chain Monte Carlo samples and apply a thinning parameter of 2^7 to mitigate correlations within the sample chain.

For example, we use this procedure to sample a large number of possible physical density matrices $\{\rho_{\text{BI},i}\}$ and compute their fidelities $F_i = (\text{tr}(\sqrt{\sqrt{\rho_{\text{BI},i}}\,\rho_{\text{tar}}\,\sqrt{\rho_{\text{BI},i}}}))^2$ to a target state ρ_{tar}. The fidelity and its error presented in the main text are the average fidelity and its standard deviation.

The quantum state reconstruction and Bayesian inference routines used in that work are available on GitHub, github.com/Qcrew/Valadares-Dorogov-FAR, along with the raw experimental data (averaged).

X. PROTOCOL SIMULATION AND ERROR BUDGET

We estimate the effect of different error sources over the resonant control protocol by solving the master equation of the system.

First, we simulate the state preparation of states $|\psi_1\rangle = \frac{1}{\sqrt{2}}\left(|0\rangle + |3\rangle\right)$ and $|\psi_2\rangle = \frac{1}{2}|0\rangle + \frac{\sqrt{3}}{\sqrt{8}}\left(i|2\rangle + |4\rangle\right)$ using sequential gaussian pulses for each transition. The system Hamiltonian was reconstructed using the experimentally calibrated transitions from Tab. III. The cavity lifetime $T_{1,\text{cav}}$, transmon lifetime T_1 and pure dephasing $T_\phi = \left(\frac{1}{T_2} - \frac{1}{2T_1}\right)^{-1}$ are implemented with the respective jump operators. The adiabatic decoupling is taken as ideal and implemented with a change of basis operation. The Wigner tomography executed in the dispersive regime is also reproduced in simulation with experimental parameters, namely a dispersive shift $\chi/2\pi = 1.62\,\text{MHz}$, a parity-mapping time of 272 ns and gaussian $\pi/2$ pulses with $\sigma_{\pi/2}$ of 8 ns and total duration of 4σ. The simulated tomography is then rescaled following the amplitude of the Wigner function of vacuum obtained with consistent simulation parameters. The state fidelity is then estimated from density matrix reconstruction following the procedure described in Sec. IX.

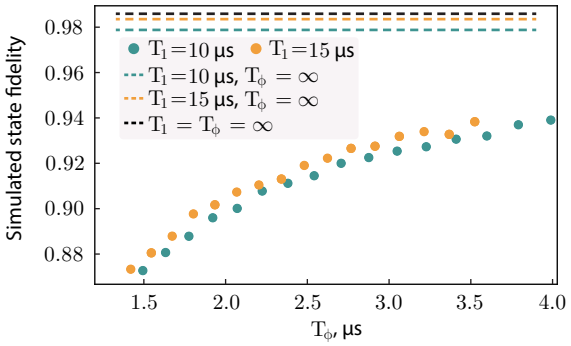

FIG. S9. **Simulated state preparation fidelities.** Simulated state fidelity of $|\psi_1\rangle = \frac{1}{\sqrt{3}}\left(|0\rangle + |3\rangle\right)$ as a function of transmon T_1 and T_ϕ.

The state preparation is simulated for transmon $T_1 = 10\,\mu\text{s}$ and $15\,\mu\text{s}$, and T_2 in the $[1.3, 2.8]$ μs range. The cavity lifetime is fixed at $T_{1,\text{cav}} = 500\,\mu\text{s}$. We first identify that the transmon is highly sensitive to changes in dephasing, as seen from the reconstructed fidelity as function of T_ϕ in Fig. S9: the fidelity of $|\psi_1\rangle$ varies in a large range $[87.2\,\%, 93.8\,\%]$ ($[87.3\,\%, 93.8\,\%]$) for $T_1 = 10\,\mu\text{s}$ ($15\,\mu\text{s}$). These values also show the protocol is weakly

sensitive to variations in transmon T_1 in this parameter range. Similar conclusions about T_1 and T_2 sensitivity can be drawn for state $|\psi_2\rangle$. Simulations with $T_2 = 2.7\,\mu$s and $T_1 = 15\,\mu$s ($T_\phi \approx 2.97\,\mu$s) lead to 93.2 % and 87.7 % for states $|\psi_1\rangle$ and $|\psi_2\rangle$, respectively, reproducing well the experimental fidelities of 93 ± 3 % and 89 ± 2 %.

Included error sources	$\|\psi_1\rangle$ fid. (%)	$\|\psi_2\rangle$ fid. (%)
Finite pulse length	98.4	95.1
+ T_1	98.3	94.4
+ T_ϕ	93.2	87.7

TABLE IV. **Error budget for state preparation.** State fidelity for $|\psi_1\rangle = \frac{1}{\sqrt{2}}\big(|0\rangle + |3\rangle\big)$ and $|\psi_2\rangle = \frac{1}{2}|0\rangle + \frac{\sqrt{3}}{\sqrt{8}}\big(i|2\rangle + |4\rangle\big)$ states with progressive addition of error sources.

We calculate the fidelities of $|\psi_1\rangle$ and $|\psi_2\rangle$ while progressively including more sources of error in the simulation (Tab. IV). The results indicate that the dephasing T_ϕ has the largest impact on state preparation fidelity, followed by coherent errors due to finite pulse length, and transmon T_1, in that order. From these simulations, we expect that the quality of state preparation can be significantly enhanced even with modest improvements in the transmon T_ϕ.

We simulate the Givens rotations between Fock states $|1\rangle$ and $|4\rangle$ using the same procedure, with the addition of the optimised $|1+\rangle \leftrightarrow |3-\rangle$ state transfer drive. The simulated cavity photon distributions are compared with the experimental reconstructed density matrix in Fig. 4c in the main text, showing a close match.

Simulations indicate that the experimental state fidelities after Givens rotations are significantly affected by coherent errors. When neglecting the transmon T_1 and T_2, the state transfer $|1+\rangle \rightarrow |3-\rangle$ shows a fidelity of 95.0 % when the system is initialised in $|1+\rangle$. For the same drive, the returning $|3-\rangle \rightarrow |1+\rangle$ path shows a fidelity of 85.8 % when the system is initialised in $|3-\rangle$. We attribute these imperfections to the mismatch between the ideal Jaynes-Cummings model used in the drive optimization and the experimental Hamiltonian parameters, which leads to a difference on the order of ≈ 1 MHz in the frequencies of higher transitions. We expect that further improvements in our calibration and optimization methods will render significant improvement in the Givens rotations fidelities.

[1] J. Koch, T. M. Yu, J. Gambetta, A. A. Houck, D. I. Schuster, J. Majer, A. Blais, M. H. Devoret, S. M. Girvin, and R. J. Schoelkopf, Charge-insensitive qubit design derived from the cooper pair box, Physical Review A—Atomic, Molecular, and Optical Physics **76**, 042319 (2007).

[2] M. Hutchings, J. B. Hertzberg, Y. Liu, N. T. Bronn, G. A. Keefe, M. Brink, J. M. Chow, and B. Plourde, Tunable superconducting qubits with flux-independent coherence, Physical Review Applied **8**, 044003 (2017).

[3] X. You, J. A. Sauls, and J. Koch, Circuit quantization in the presence of time-dependent external flux, Physical Review B **99**, 174512 (2019).

[4] Y. Lu, T. Zhao, A. Vallières, K. C. Smith, D. Weiss, X. You, Y. Zhang, S. Ganjam, A. Maiti, J. W. Garmon, *et al.*, Systematic construction of time-dependent hamiltonians for microwave-driven josephson circuits, arXiv preprint arXiv:2512.20743 (2025).

[5] F. W. Strauch, All-resonant control of superconducting resonators, Physical Review Letters **109**, 210501 (2012).

[6] B. M. Terhal and D. Weigand, Encoding a qubit into a cavity mode in circuit qed using phase estimation, Physical Review A **93**, 012315 (2016).

[7] C. Joshi, J. Larson, and T. P. Spiller, Quantum state engineering in hybrid open quantum systems, Physical Review A **93**, 043818 (2016).

[8] G. Wang, R. Xiao, H. Shen, C. Sun, and K. Xue, Simulating anisotropic quantum rabi model via frequency modulation, Scientific reports **9**, 4569 (2019).

[9] L. J. Henderson, R. Goel, and S. Shrapnel, Quantum kernel machine learning with continuous variables, Quantum **8**, 1570 (2024).

[10] A. Tolstobrov, G. Fedorov, S. Sanduleanu, S. Kadyrmetov, A. Vasenin, A. Bolgar, D. Kalacheva, V. Lubsanov, A. Dorogov, J. Zotova, *et al.*, Hybrid quantum learning with data reuploading on a small-scale superconducting quantum simulator, Physical Review A **109**, 012411 (2024).

[11] M. Reed, *Entanglement and quantum error correction with superconducting qubits* (Lulu. com, 2013).

[12] O. Gargiulo, S. Oleschko, J. Prat-Camps, M. Zanner, and G. Kirchmair, Fast flux control of 3d transmon qubits using a magnetic hose, Applied Physics Letters **118** (2021).

[13] F. Valadares, N.-N. Huang, K. T. N. Chu, A. Dorogov, W. Chua, L. Kong, P. Song, and Y. Y. Gao, On-demand transposition across light-matter interaction regimes in bosonic cqed, Nature Communications **15**, 5816 (2024).

[14] D. G. Atanasova, I. Yang, T. Hönigl-Decrinis, D. Gusenkova, I. Pop, and G. Kirchmair, In situ tunable interaction with an invertible sign between a fluxonium and a post cavity, PRX Quantum **6**, 020318 (2025).

[15] D. M. Pozar, *Microwave engineering: theory and techniques* (John Wiley & Sons, 2021).

[16] Z. Li, E. Gupta, F. Zhao, R. Banerjee, Y. Lu, T. Roy, A. Oriani, A. Vrajitoarea, S. Chakram, and D. I. Schuster, A Cascaded Random Access Quantum Memory (2025), arXiv:2503.13953.

[17] F. Lecocq, C. Naud, I. M. Pop, Z.-H. Peng, I. Matei, T. Crozes, T. Fournier, W. Guichard, and O. Buisson, Novel e-beam lithography technique for in-situ junction fabrication: the controlled undercut, arXiv preprint arXiv:1101.4576 (2011).

[18] A. Copetudo, C. Y. Fontaine, F. Valadares, and Y. Y. Gao, Shaping photons: Quantum information processing with bosonic cqed, Applied Physics Letters **124** (2024).

[19] X. Pan, T. Krisnanda, A. Duina, K. Park, P. Song, C. Y. Fontaine, A. Copetudo, R. Filip, and Y. Y. Gao, Realization of versatile and effective quantum metrology using

a single bosonic mode, PRX Quantum **6**, 010304 (2025).
[20] O. Milul, B. Guttel, U. Goldblatt, S. Hazanov, L. M. Joshi, D. Chausovsky, N. Kahn, E. çiftyürek, F. Lafont, and S. Rosenblum, Superconducting cavity qubit with tens of milliseconds single-photon coherence time, PRX Quantum **4**, 030336 (2023).
[21] L. V. Krayzman, *Thin-film 3D resonators for superconducting quantum circuits*, Ph.D. thesis, Yale University (2022).
[22] S. Krastanov, V. V. Albert, C. Shen, C.-L. Zou, R. W. Heeres, B. Vlastakis, R. J. Schoelkopf, and L. Jiang, Universal control of an oscillator with dispersive coupling to a qubit, Physical Review A **92**, 040303(R) (2015).
[23] R. W. Heeres, B. Vlastakis, E. Holland, S. Krastanov, V. V. Albert, L. Frunzio, L. Jiang, and R. J. Schoelkopf, Cavity State Manipulation Using Photon-Number Selective Phase Gates, Physical Review Letters **115**, 137002 (2015).
[24] R. W. Heeres, P. Reinhold, N. Ofek, L. Frunzio, L. Jiang, M. H. Devoret, and R. J. Schoelkopf, Implementing a universal gate set on a logical qubit encoded in an oscillator, Nature Communications **8**, 94 (2017).
[25] A. Eickbusch, V. Sivak, A. Z. Ding, S. S. Elder, S. R. Jha, J. Venkatraman, B. Royer, S. M. Girvin, R. J. Schoelkopf, and M. H. Devoret, Fast universal control of an oscillator with weak dispersive coupling to a qubit, Nature Physics **18**, 1464–1469 (2022).
[26] W.-L. Ma, S. Puri, R. J. Schoelkopf, M. H. Devoret, S. M. Girvin, and L. Jiang, Quantum control of bosonic modes with superconducting circuits, Science Bulletin **66**, 1789 (2021).
[27] A. Blais, A. L. Grimsmo, S. M. Girvin, and A. Wallraff, Circuit quantum electrodynamics, Reviews of Modern Physics **93**, 025005 (2021).
[28] C. K. Law and J. H. Eberly, Arbitrary control of a quantum electromagnetic field, Physical review letters **76**, 1055 (1996).
[29] M. Hofheinz, H. Wang, M. Ansmann, R. C. Bialczak, E. Lucero, M. Neeley, A. O'connell, D. Sank, J. Wenner, J. M. Martinis, *et al.*, Synthesizing arbitrary quantum states in a superconducting resonator, Nature **459**, 546 (2009).
[30] F. W. Strauch, All-Resonant Control of Superconducting Resonators, Physical Review Letters **109**, 210501 (2012).
[31] A. Mezzacapo, U. Las Heras, J. Pedernales, L. DiCarlo, E. Solano, and L. Lamata, Digital quantum rabi and dicke models in superconducting circuits, Scientific reports **4**, 7482 (2014).
[32] A. M. Eriksson, T. Sépulcre, M. Kervinen, T. Hillmann, M. Kudra, S. Dupouy, Y. Lu, M. Khanahmadi, J. Yang, C. Castillo-Moreno, *et al.*, Universal control of a bosonic mode via drive-activated native cubic interactions, Nature Communications **15**, 2512 (2024).
[33] M. H. Michael, M. Silveri, R. Brierley, V. V. Albert, J. Salmilehto, L. Jiang, and S. M. Girvin, New class of quantum error-correcting codes for a bosonic mode, Physical Review X **6**, 031006 (2016).
[34] N. Didier, E. A. Sete, M. P. da Silva, and C. Rigetti, Analytical modeling of parametrically modulated transmon qubits, Physical Review A **97**, 022330 (2018).
[35] Y. Lu, A. Maiti, J. W. O. Garmon, S. Ganjam, Y. Zhang, J. Claes, L. Frunzio, S. M. Girvin, and R. J. Schoelkopf, High-fidelity parametric beamsplitting with a parity-protected converter, Nature Communications **14**, 5767 (2023).
[36] J. A. Smolin, J. M. Gambetta, and G. Smith, Efficient method for computing the maximum-likelihood quantum state from measurements with additive gaussian noise, Physical review letters **108**, 070502 (2012).
[37] R. Blume-Kohout, Optimal, reliable estimation of quantum states, New Journal of Physics **12**, 043034 (2010).
[38] L. Knips, C. Schwemmer, N. Klein, J. Reuter, G. Tóth, and H. Weinfurter, How long does it take to obtain a physical density matrix?, arXiv preprint arXiv:1512.06866 (2015).
[39] J. M. Lukens, K. J. Law, A. Jasra, and P. Lougovski, A practical and efficient approach for bayesian quantum state estimation, New Journal of Physics **22**, 063038 (2020).